# Heterogeneous integration of singlecrystalline complex-oxide membranes

https://doi.org/10.1038/s41586-020-1939-z

Received: 30 June 2019

Accepted: 4 December 2019

Published online: 5 February 2020

Hyun S. Kum<sup>1,15</sup>, Hyungwoo Lee<sup>2,15</sup>, Sungkyu Kim<sup>1,15</sup>, Shane Lindemann<sup>2,15</sup>, Wei Kong<sup>1</sup>, Kuan Qiao<sup>1</sup>, Peng Chen<sup>1</sup>, Julian Irwin<sup>3</sup>, June Hyuk Lee<sup>4</sup>, Saien Xie<sup>5,6</sup>, Shruti Subramanian<sup>7</sup>, Jaewoo Shim<sup>1</sup>, Sang-Hoon Bae<sup>1</sup>, Chanyeol Choi<sup>8</sup>, Luigi Ranno<sup>1,9</sup>, Seungju Seo<sup>1</sup>, Sangho Lee<sup>1,9</sup>, Jackson Bauer<sup>9</sup>, Huashan Li<sup>10</sup>, Kyusang Lee<sup>11,12</sup>, Joshua A. Robinson<sup>7</sup>, Caroline A. Ross<sup>9</sup>, Darrell G. Schlom<sup>5,6</sup>, Mark S. Rzchowski<sup>3</sup>, Chang-Beom Eom<sup>2,\*</sup> & Jeehwan Kim<sup>1,9,13,14,\*</sup>

Complex-oxide materials exhibit a vast range of functional properties desirable for next-generation electronic, spintronic, magnetoelectric, neuromorphic, and energy conversion storage devices<sup>1-4</sup>. Their physical functionalities can be coupled by stacking layers of such materials to create heterostructures and can be further boosted by applying strain<sup>5-7</sup>. The predominant method for heterogeneous integration and application of strain has been through heteroepitaxy, which drastically limits the possible material combinations and the ability to integrate complex oxides with mature semiconductor technologies. Moreover, key physical properties of complex-oxide thin films, such as piezoelectricity and magnetostriction, are severely reduced by the substrate clamping effect. Here we demonstrate a universal mechanical exfoliation method of producing freestanding single-crystalline membranes made from a wide range of complex-oxide materials including perovskite, spinel and garnet crystal structures with varying crystallographic orientations. In addition, we create artificial heterostructures and hybridize their physical properties by directly stacking such freestanding membranes with different crystal structures and orientations, which is not possible using conventional methods. Our results establish a platform for stacking and coupling three-dimensional structures, akin to two-dimensional material-based heterostructures, for enhancing device functionalities<sup>8,9</sup>.

Traditionally, heterogeneous coupling and control of strain for crystalline films are carried out through heteroepitaxy on lattice-mismatched substrates<sup>10,11</sup>. Epitaxial methods, however, have fundamental limitations that prevent the unrestricted manipulation, integration and utilization of these materials. First, heteroepitaxy occurs only for different materials that have a lattice constant or crystal structure within a certain threshold. Thus, heterostructuring via epitaxy is allowed only for relatively limited material systems. Moreover, the degree of strain that can be applied to an epitaxial layer is fixed by pseudomorphic epitaxial conditions. Second, the epitaxial film is clamped by the substrate, constraining several important properties. For example, the piezoelectric and magnetostrictive responses are dampened by approximately an order of magnitude by the substrate clamping effect, reducing their sensitivity and maximum response<sup>12</sup>. Third, epitaxial growth typically requires elevated temperatures, often preventing the epitaxial integration of materials that are stable in very different environments or are thermodynamically unstable when in contact with each other; such instability typically precludes the epitaxial integration of complex oxides with mainstream semiconductor materials. Thus, it has been extremely challenging to form heterostructures between materials with large lattice mismatch or between materials chosen solely for the desired properties they would bring to an artificial heterostructure, and it is even more challenging to unclamp epitaxial films from the substrate. Freestanding heterostructures without any limitations in crystal structures are often achieved in two-dimensional (2D) material systems by stacking ultrathin layers (a few atoms thick) of 2D materials<sup>13</sup>, and the concepts of layer transfer of single materials or of various individual devices composed of nanomaterials onto foreign substrates have been demonstrated in the past<sup>14-16</sup>. However, artificial heterostructuring of multiple single-crystalline membranes and robust physical coupling, experimentally demonstrated here, have been elusive. Although chemical lift-off of oxide materials has

Department of Mechanical Engineering, Massachusetts Institute of Technology, Cambridge, MA, USA. Department of Materials Science and Engineering, University of Wisconsin-Madison, Madison, WI, USA. Department of Physics, University of Wisconsin-Madison, Madison, WI, USA. Neutron Science Division, Korea Atomic Energy Research Institute, Daejeon, South Korea. Department of Materials Science and Engineering, Cornell University, Ithaca, NY, USA. Kavli Institute at Cornell for Nanoscale Science, Ithaca, NY, USA. Department of Materials Science and Engineering, The Pennsylvania State University, University Park, PA, USA. Department of Electrical Engineering and Computer Science, Massachusetts Institute of Technology, Cambridge, MA, USA. Department of Materials Science and Engineering, Massachusetts Institute of Technology, Cambridge, MA, USA. Science and Engineering, University of Virginia, Charlottesville, VA, USA. Science and Engineering, University of Virginia, Charlottesville, VA, USA. Research Laboratory of Electronics, Massachusetts Institute of Technology, Cambridge, MA, USA. Massachusetts Institute of Technology, Cambridge, MA, USA. Science and Engineering, University of Virginia, Charlottesville, VA, USA. Science and Engineering, University of Virginia, Charlottesville, VA, USA. Science and Engineering, University of Virginia, Charlottesville, VA, USA. Science and Engineering, University of Virginia, Charlottesville, VA, USA. Science and Engineering, University of Virginia, Charlottesville, VA, USA. Science and Engineering, University of Virginia, Charlottesville, VA, USA. Science and Engineering, University of Virginia, Charlottesville, VA, USA. Science and Engineering, University of Virginia, Charlottesville, VA, USA. Science and Engineering, University of Virginia, Charlottesville, VA, USA. Science and Engineering University of Virginia, Charlottesville, VA, USA. Science and Engineering University of Virginia, Charlottesville, VA, USA. Science and Engineering University of Virginia, Charlottesville, VA, US

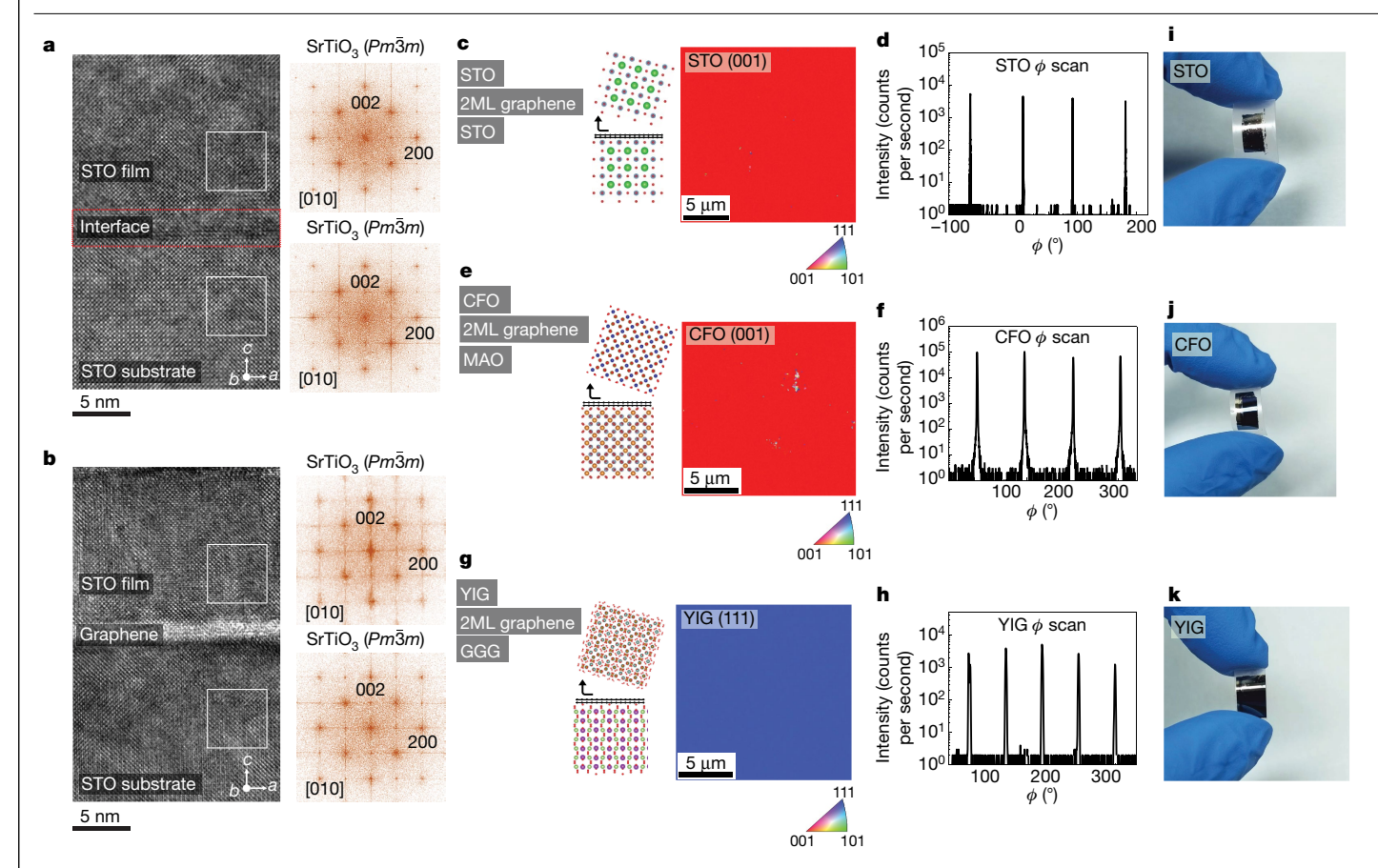


Fig. 1 | Epitaxial lift-off of complex-oxide membranes on graphene-coated substrates. Cross-sectional TEM of STO film grown on a graphene-coated STO substrate without (a) and with (b) a graphene protection layer. White boxes indicate the fast Fourier transform areas, which confirm the crystallinity of each epitaxial region in comparison to the substrate. c, EBSD of the exfoliated STO membrane, confirming the single-crystalline out-of-plane (001) orientation. 2ML, two monolayers. **d**, Asymmetric  $\phi$  scan of the STO membrane measured by high-resolution X-ray diffraction. EBSD and

asymmetric  $\phi$  scans of CFO (100) (**e**, **f**) and YIG (111) (**g**, **h**) membranes, showing single-crystallinity with uniform out-of-plane orientation and no in-plane rotation. i-k, Photographs of the exfoliated oxide membranes (100 nm of STO (i), CFO (j) and YIG (k)) supported on thermal release tape. The strain applied to the film in the figure with a bending radius of 1.5 cm is not sufficient to crack the films  $^{42,43}$ . The strain increases with thickness and for the 100-nmthick films with 1.5 cm bending radius, the strain is around 0.1%, which is much smaller than the critical cracking strain of about 1%.

been reported<sup>17-21</sup>, this method is applicable only to a limited range of material systems owing to the lattice mismatch and etch selectivity constraints between the epitaxial layer, sacrificial layer and the substrate. Additionally, slow release rate is generally a well known shortcoming of chemical lift-off for larger substrates.

Here we prepare artificial complex-oxide heterostructure stacks using mechanical lift-off techniques, in which the epitaxial oxide films are instantly separated from weakened epitaxial interfaces to form freestanding single-crystalline membranes. These techniques can, in theory, be universally applied to prepare freestanding membranes across a broad range of crystal structures (for example, perovskite, spinel and garnet) with the potential capability of reusing the host oxide substrate. We now demonstrate freestanding membranes made from several important oxide structures including archetypal perovskite SrTiO<sub>3</sub> (STO), perovskite BaTiO<sub>3</sub> (BTO), spinel CoFe<sub>2</sub>O<sub>4</sub> (CFO), garnet Y<sub>3</sub>Fe<sub>5</sub>O<sub>12</sub> (YIG) and a perovskite of complex composition Pb(Mg<sub>1/3</sub>Nb<sub>2/3</sub>)O<sub>3</sub>-PbTiO<sub>3</sub> (PMN-PT). Single-crystalline STO, BTO, CFO and YIG were remote-epitaxially (that is, by epitaxial growth of thin films seeded by the underlying substrate through a few layers of graphene)<sup>22,23</sup> grown on graphene-coated STO, MgAl<sub>2</sub>O<sub>4</sub> (MAO) and Gd<sub>3</sub>Ga<sub>5</sub>O<sub>12</sub> (GGG) substrates, respectively, followed by mechanical exfoliation. In addition, we demonstrate single-crystalline freestanding membranes of PMN-PT that are grown via sputtering, which damages graphene<sup>24</sup>. This was enabled by discovering that SrRuO<sub>3</sub> (SRO) can provide a weak interface with PMN-PT, allowing PMN-PT films to be mechanically released precisely at the PMN-PT/SRO interface without use of graphene. From these freestanding membranes, we fabricated various heterostructures with the goal of coupling the unique properties of the component materials by stacking them directly (that is, there is nothing between the layers). Enhanced magnetoelectric coupling has been observed by stacking magnetostrictive CFO and piezoelectric PMN-PT, because their physical properties can be greatly enhanced in freestanding form by being declamped from the substrate. We also demonstrate magnetostatic and magnetoelastic coupling in a CFO/YIG membrane heterostructure. More importantly, we verified the electrical coupling of graphene sandwiched between freestanding CFO and YIG membranes by tracing the Fermi level shift with respect to the Dirac point of graphene. Our findings advance oxide research by allowing unrestricted integration of single-crystalline, dissimilar, complex-oxide membranes into elaborate heterostructures unattainable by epitaxy and chemical lift-off methods, which opens up opportunities to produce unprecedented three-dimensional (3D) het $erostructures formed from various freestanding 2D \, or \, 3D \, membranes.$ 

We first studied the growth dynamics of STO films on graphenecoated STO (001) substrates (see Supplementary Information for details of the transfer process). Our density functional theory calculation suggests that atomic potential fields can penetrate completely through bilayer graphene and partially through trilayer graphene (Extended Data Fig. 1), thus allowing successful remote epitaxy up to two monolayers of graphene interlayers. Our pulsed-laser-deposition experimental results precisely followed our prediction: single-crystalline STO films

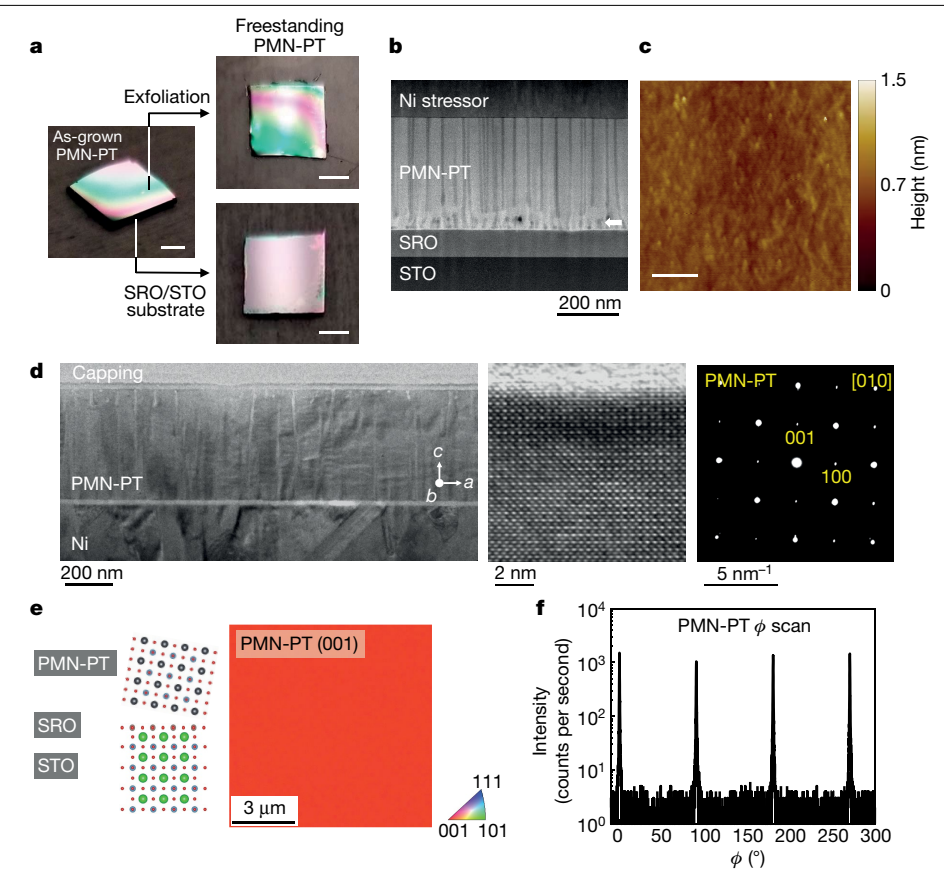
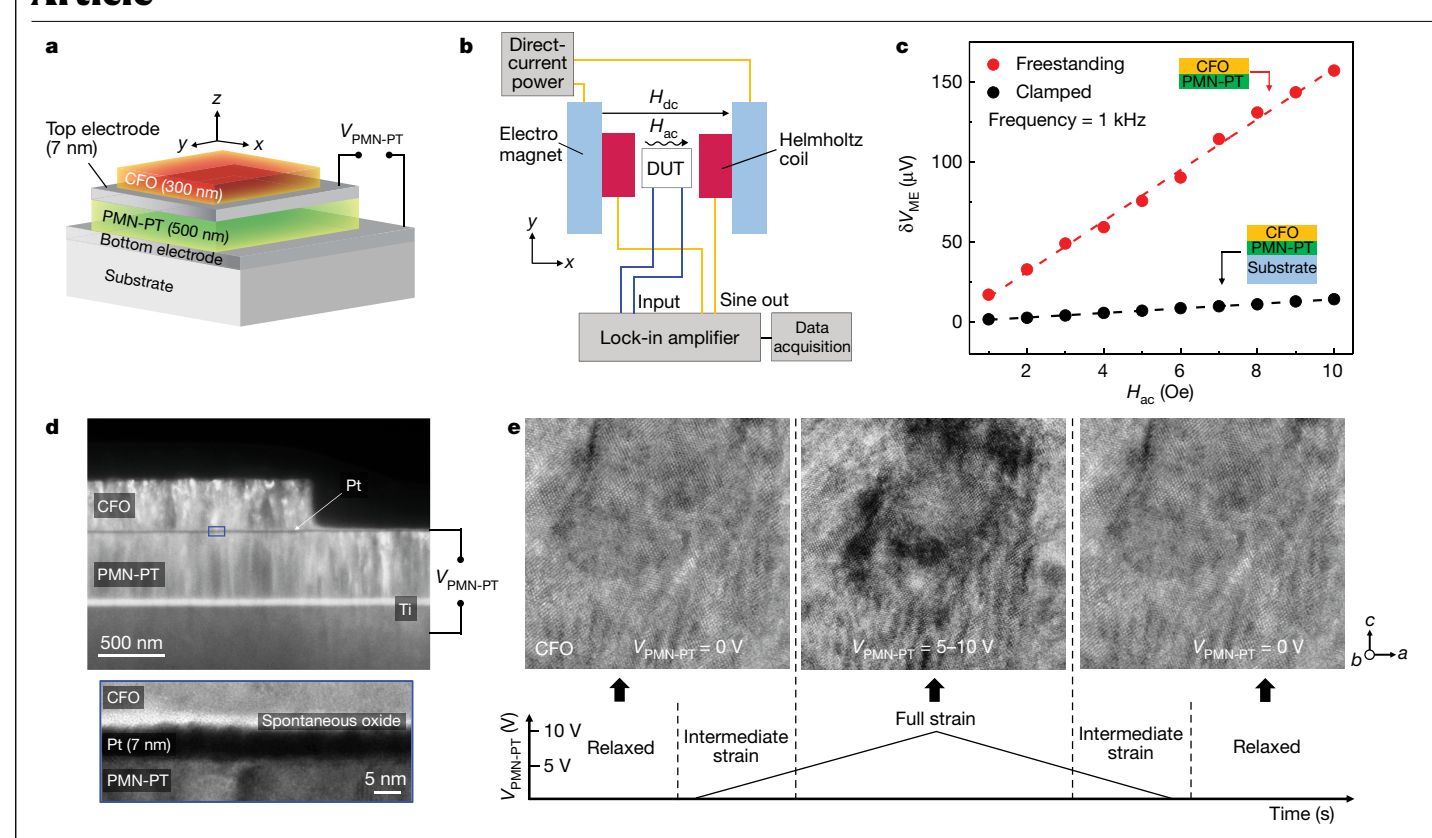


Fig. 2 | Precise epitaxial interface separation of PMN-PT on a SRO/STO substrate. a, Photograph of as-grown PMN-PT on a SRO/STO substrate (left), SRO/STO substrate after PMN-PT exfoliation (bottom right), and exfoliated PMN-PT membrane (top right). The scale bar indicates 2 mm. b, HAADF-STEM  $image \, of \, the \, PMN-PT/SRO/STO \, interface, with \, high-stress \, Ni \, (100 \, nm)$ deposited on top. c, AFM of the SRO/STO substrate surface after exfoliating the PMN-PT. The scale bar indicates 5 µm. d, Cross-sectional TEM (left) of the exfoliated PMN-PT using a Ti (30 nm)/Ni (3 µm) metal stressor layer, verifying

the integrity of the PMN-PT crystallinity after exfoliation. Needle-like contrast areas are caused by slight variations in composition and phase that are attributable to misfit strain<sup>44</sup>. Representative high-resolution TEM (middle) and selective-area diffraction (right) images are also shown, verifying the single-crystalline nature of the exfoliated PMN-PT membrane. e, f, EBSD (e) and asymmetric  $\phi$  scan (f) of the exfoliated PMN-PT membrane, showing highquality single-crystallinity and no in-plane rotation.

were successfully grown through bilayer graphene interlayers proving successful seeding from the STO substrates through graphene<sup>25</sup> (see Methods for epitaxy conditions). In situ high-pressure reflection high-energy electron diffraction (RHEED) during growth also showed clear intensity oscillations and crystallinity of the film during growth (Extended Data Fig. 2). In contrast to epitaxy of semiconductor compounds from groups III-V and III-nitrides on graphene where the adatoms or substrate do not react with graphene, it is crucial to avoid oxidation of graphene for epitaxy of oxides to ensure the release of remote epitaxial STO<sup>26</sup>. Initially, we were unable to exfoliate the STO films grown in a conventional oxygen overpressure owing to the graphene being etched during the nucleation stage from the substrate as evidenced by the absence of graphene in cross-sectional transmission electron microscopy (TEM) (Fig. 1a). To protect the graphene, we deposited an ultrathin STO buffer (about 5-10 nm), which is not grown in a conventional oxygen overpressure, but under vacuum ( $<5 \times 10^{-6}$  torr). By applying this buffer, we were able to preserve the graphene (Fig. 1b), resulting in successful production of freestanding STO membranes (Extended Data Fig. 3). An electron backscatter diffraction (EBSD) map of the STO film (Fig. 1c) showed (001) cubic orientation over a large area. Additionally, azimuthal X-ray diffraction  $\phi$  scanning confirmed in-plane single-crystallinity without any rotated domains (Fig. 1d). We also verified, via electron energy loss spectroscopy, that further growth of STO in an oxygen overpressure effectively corrects the oxygen stoichiometry of the entire STO film, even the region grown under vacuum (Extended Data Fig. 4). We note that because the STO substrate is also a source of oxygen<sup>27</sup>, the exfoliation area yield of the sample with one monolayer of graphene is low compared to the exfoliation area yield of samples with two or more graphene layers (Supplementary Fig. 1). Through these findings, we concluded that two graphene layers are optimal to achieve the highest ratio of crystal quality to exfoliation vield.

As representative cases for spinel and garnet oxides, we grew spinel CFO and garnet YIG on graphene-coated MAO (001) and GGG (111) substrates, respectively. Single-crystallinity of the grown film was again verified by EBSD and high-resolution X-ray diffraction (Fig. 1e-h). The magnetization values of freestanding CFO and YIG were within a reasonable range of the bulk values, indicating the good quality of freestanding single-crystalline membranes (Supplementary Fig. 2). We carried out cross-sectional transmission electron microscope (TEM) measurements on the exfoliated CFO membrane to confirm the crystallinity at an atomic scale. Within the single-crystalline matrix, we were able to observe localized polycrystalline domains (Extended Data Fig. 5). The case is similar for other remote epitaxial membranes (see Extended Data Fig. 3). These polycrystalline domains are probably caused by regions of non-uniform graphene thickness or organic/metal residues left from graphene transfer and due to the high sticking coefficient of oxide adatoms<sup>28</sup>. Thus, the quality of the transferred graphene on the substrate determines the exfoliation area and crystallinity of the epitaxial film. Regardless, applying a thin protection layer before growing in an oxygen environment is effective for all materials explored here: all epitaxial films were successfully released from the substrate.



 $Fig.\,3\,|\,Heterogeneous\,integration\,of\,CFO\,and\,PMN-PT\,membranes\,for$ strain-mediated thin-film magnetoelectrically coupled heterostructure.

a, Device schematic of the CFO/PMN-PT magnetoelectric device. The CFO has an area of  $4\times3\,\text{mm}^2$  and a thickness of 300 nm. The PMN-PT has an area of 5×5 mm<sup>2</sup> and a thickness of 500 nm. For the clamped device, the substrate is STO and the bottom electrode is SRO. For the freestanding membrane device, the substrate is PDMS and the bottom electrode is Ti. b, Schematic of the setup to measure the magnetic-field-induced voltage across the PMN-PT. A small alternating-current magnetic field is supplied by a Helmholtz coil and a directcurrent magnetic field is provided by an electromagnet. The magnetic-field direction is applied parallel to the sample. The voltage generated across the PMN-PT membrane is measured as a function of the alternating-current magnetic-field amplitude with a lock-in amplifier. DUT stands for device under test. **c**, The voltage induced across the PMN-PT ( $\delta V_{\text{ME}}$ ) as a function of the alternating-current magnetic field strength at a frequency of 1 kHz. The inset shows schematics of the freestanding and the clamped devices. d, Crosssectional TEM image of the CFO/PMN-PT membrane heterostructure. A thin Pt (7 nm) film was deposited before transferring the CFO as the top contact to PMN-PT. The blue box shows a zoomed-in TEM of the CFO/Pt/PMN-PT interface, showing that an oxide bonding layer has formed spontaneously. e, In situ TEM of CFO as a function of applied voltage across the PMN-PT membrane. The strain generated by applying a voltage across the PMN-PT is transferred to the CFO layer, which induces a large change in strain contrast. The movement of the strain contrast can be more clearly seen in the Supplementary Video.

The resulting flexible STO, CFO and YIG membranes with thicknesses of 100 nm are shown in Fig. 1i-k, supported by a flexible handling tape. Moreover, we verified the compatibility of this process using molecular-beam epitaxy (MBE), another technique often used to grow single-crystalline complex-oxide films, by growing BTO on graphenecoated STO substrates and exfoliating the BTO film. Single-crystalline BTO membranes were produced, similar to the results obtained by pulsed-laser deposition (Extended Data Fig. 6).

We also discovered that the bilayer graphene interlayer not only enhances exfoliation yield, but also minimizes damage to the substrate upon peeling, thus promoting reusability of the substrates. We have successfully obtained multiple CFO freestanding membranes by reusing a single graphene-coated MAO substrate three times. The magnetic hysteresis measured from freestanding CFO using vibrating sample magnetometry was consistent throughout each exfoliation, confirming the reusability of the MAO substrate. To the best of our knowledge, our demonstration is the first to show wafer reusability for producing freestanding complex oxides, which drastically reduces production costs for applications (see Extended Data Fig. 7 and Supplementary Fig. 3 for details).

We have further broadened our mechanical exfoliation technique to oxides with more complex compositions such as PMN-PT. Singlecrystalline PMN-PT films were prepared previously by sputtering <sup>24,29</sup>.

Consequently, remote epitaxy strategies cannot be applied owing to the harsh plasma overpressure that rapidly etches graphene<sup>30</sup>. We discovered that PMN-PT is weakly bonded to SRO, allowing mechanical exfolia $tion \, of \, PMN\text{-}PT \, with \, near-atomic \, precision. \, For \, this, \, we \, grew \, 500\text{-}nm$ PMN-PT/100-nm SRO epitaxial heterostructures on STO substrates by sputtering without graphene, followed by the deposition of a 3–5-µm Ni stressor layer with a stress of around 800 MPa. Upon mechanical exfoliation, the Ni stressor provided enough strain energy to guide the crack propagation precisely at the PMN-PT/SRO interface with minimum damage to the substrate (Fig. 2a). As shown in the high-angle annular dark-field (HAADF) scanning transmission electron microscope (STEM) image in Fig. 2b, the PMN-PT/SRO interface is severely strained whereas the SRO/STO interface is pristine. After depositing high-stress Ni on PMN-PT, indications of an increased strain at the interface was observed. Our geometric phase analysis revealed that a closely spaced network of misfit dislocations (spaced about 20 nm apart) applies strain at the interface while the Ni stressor provides additional stress to the PMN-PT/SRO interface (Extended Data Fig. 8). We speculate that the resulting concentrated strain field at the PMN-PT/SRO interface provides a sufficiently weak interface to allow atomically precise crack propagation. We have reproducibly verified the precise crack propagation through the PMN-PT/SRO interface by atomic force microscopy (AFM) on the exfoliated SRO surface, which showed a root-mean-square

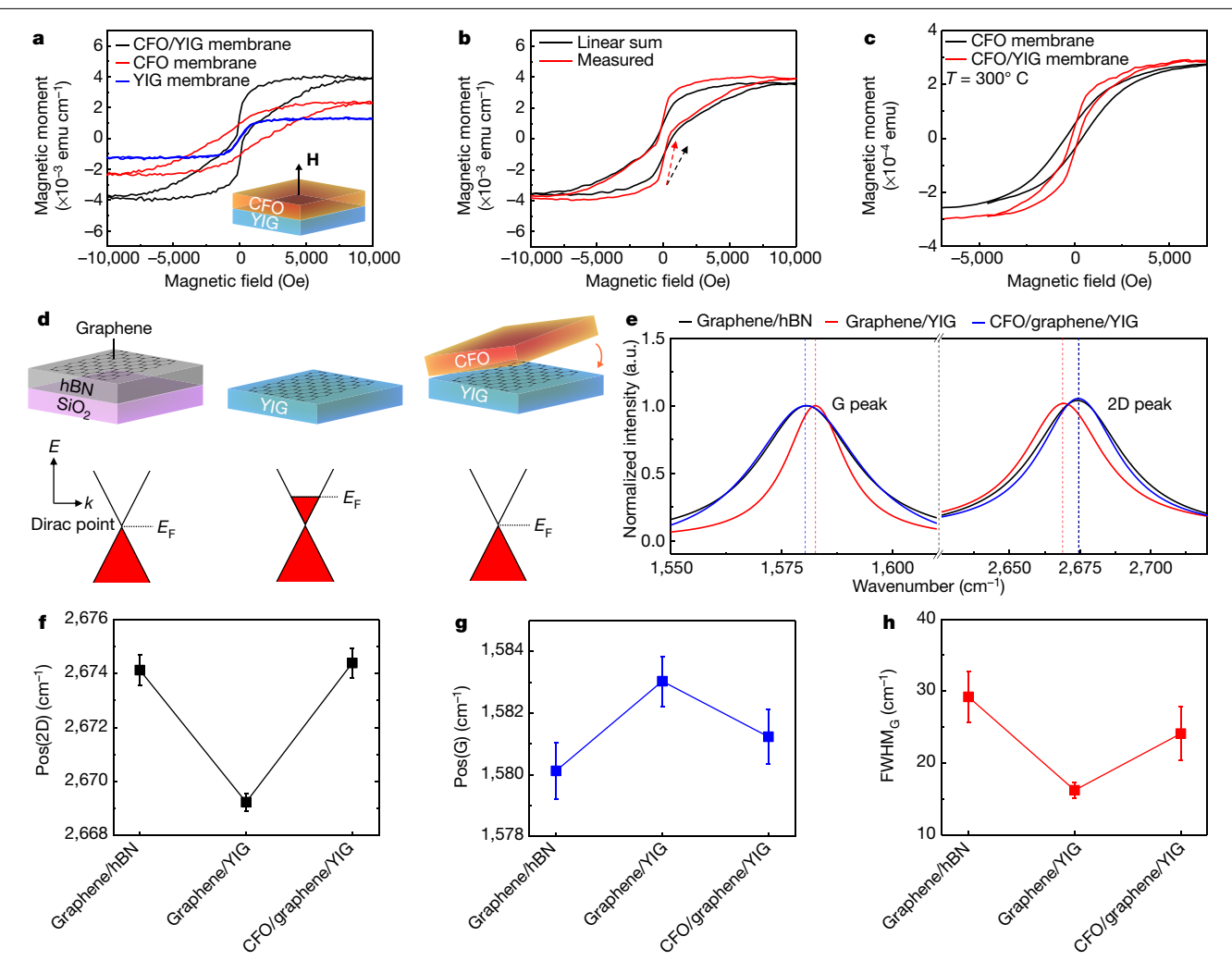


**Fig. 4** | **Electrical, magnetostatic and magnetoelastic coupling between 3D and 2D materials. a**, Out-of-plane magnetic hysteresis of CFO membrane, YIG membrane, and CFO/YIG membrane heterostructures measured at room temperature. The YIG and CFO membranes individually show hysteresis loops with an in-plane easy axis resulting from shape anisotropy. The YIG has a low inplane coercivity of  $H_{\rm c,IP}$  = 10 Oe, the CFO is magnetically harder with  $H_{\rm c,IP}$  = 2,950 Oe (Supplementary Fig. 2), and the out-of-plane loops correspond to hard-axis loops. **b**, The linear sum of the magnetic hysteresis of individual CFO and YIG membranes compared to that of the measured CFO/YIG membrane heterostructure. emu, electromagnetic unit. **c**, Magnetic hysteresis of the CFO/YIG membrane and of just the CFO membrane at 300 °C. The YIG becomes paramagnetic and only the CFO loop remains at 300 °C. When the

heterostructure membrane is cooled back down to room temperature, full recovery of the original hysteresis is observed.  ${\bf d}$ , Schematic illustration of the electrical coupling between graphene and magnetic insulators. Graphene is undoped (the Fermi level lies at the Dirac point) on thick hBN, n-doped on YIG, and p-doped on CFO, shifting the Fermi level back to near the Dirac point when sandwiched between YIG and CFO.  ${\bf e}$ , The Raman spectra (focused on the 2D peak and the G peak) of each structure shown in  ${\bf d}$ .  ${\bf f}$ - ${\bf h}$ , The shift in the 2D peak (Pos(2D)) ( ${\bf f}$ ), the shift in the G peak (Pos(G)) ( ${\bf g}$ ) and the FWHM of the G peak (FWHM $_{\rm G}$ ) ( ${\bf h}$ ) for graphene on hBN, YIG and sandwiched between YIG and CFO membranes, respectively. The error bars indicate the standard deviation of ten measurements from different parts of the sample.

roughness of about 2 Å (Fig. 2c). Cross-sectional TEM investigation of the exfoliated PMN-PT membranes revealed high crystalline quality as well as relieved strain at the PMN-PT surface that was bonded to the SRO before exfoliation (see Fig. 2d). Single-crystallinity over a large area has been confirmed by EBSD mapping and azimuthal  $\phi$  scans (Fig. 2e, f). In TEM, diffraction patterns taken from all imaged areas showed a single (001) orientation consistent with other characterization. We note that this technique also worked for (110) PMN-PT films grown on SRO or STO (Supplementary Fig. 4). Although details of the mechanism for the weakened interface between SRO and PMN-PT still remain to be verified, this finding further broadens the range of complex-oxide material systems that can be produced as freestanding membranes and provides opportunities to develop a graphene-free layer-release process by further exploring interface strain engineering.

Next, we fabricated heterostructures by stacking our freestanding membranes where robust mechanical coupling was observed with high transfer yield (>90%). We first chose to stack CFO membranes onto PMN-PT membranes (see Supplementary Fig. 5 for the thin-film stacking procedure) to create a composite multiferroic (Fig. 3a). This composite allows (1) strain-mediated electric-field control of the magnetism in CFO or (2) magnetic-field-induced voltage generation across PMN-PT by virtue of the magnetostrictive and piezoelectric properties of CFO and PMN-PT, respectively.

We expect that the piezoelectric and magnetostrictive properties of these two films will be enhanced when both membranes are in their freestanding form given that they are thus free from the substrate clamping effect. PMN-PT is a material with remarkably high piezoelectric coefficient in its single-crystalline form 31–33, whereas CFO has a high magnetostriction coefficient 34. Thus, an enhanced strain-mediated magnetoelectric response can be expected from the stacked multiferroic heterostructure if both films are freestanding compared to when at least one of the films is clamped to the substrate. Until now,

it has only been possible to use bulk materials bonded by glue<sup>35</sup> or to grow polycrystalline films on top of piezoelectric wafers<sup>36</sup> or membranes<sup>37</sup> to realize such a hybrid structure. As expected, we observed a substantially enhanced coupling effect when both the CFO and PMN-PT were freestanding compared to that of the device where the PMN-PT was clamped to the substrate, by measuring the magnetically induced magnetoelectric coupling as shown in Fig. 3b. As shown in Fig. 3c, the freestanding CFO/PMN-PT device produces substantially larger voltage ( $\delta V_{\text{ME}}$ ) than the clamped device by more than an order of magnitude, with corresponding magnetoelectric coupling coefficients of 477 mV cm<sup>-1</sup> Oe<sup>-1</sup> and 2,675 mV cm<sup>-1</sup> Oe<sup>-1</sup> for the clamped and declamped devices, respectively. This magnetoelectric coupling coefficient is approximately an order of magnitude larger than previously reported coefficients on the same material system and comparable thickness<sup>38,39</sup>. This data indicates that strain transfer from CFO to PMN-PT is more effective for the freestanding CFO/PMN-PT heterostructure. Indeed, such excellent strain transfer between the two freestanding membranes was observed using in situ TEM (see Fig. 3d and Extended Data Fig. 9 for SEM of fabricated in situ device), showing the change in the CFO structure in response to an applied voltage (-10 V to 10 V) across the PMN-PT. We note that a bonding oxide layer was spontaneously formed between the CFO membrane and Pt layer for efficient strain transfer from the PMN-PT to the CFO (see bottom TEM image of Fig. 3d). The Supplementary Video shows the motion of the strain fringes in CFO in response to the strain induced by the biased PMN-PT underneath (see Fig. 3e for TEM images with or without bias showing the generation of strain fringes upon biasing). We were careful to prevent strain fringes from being generated owing to the sample flexing (see Methods for TEM sample preparation). The excellent strain transfer from freestanding PMN-PT to CFO was also verified by observing the large modulation of the magnetic hysteresis of CFO as a function of bias across PMN-PT, in contrast to the clamped device (see Extended Data Fig. 10). Thus, the CFO/PMN-PT device showcases an example of a 3D heterostructure where the functionality of each material is enhanced by stacking freestanding 3D membranes of the constituent materials.

We fabricated additional 3D complex-oxide heterostructures as well as 2D to 3D mixed heterostructures forming direct junctions to study the feasibility of new physical couplings that are not possible by conventional epitaxy. First, we observed clear magnetostatic coupling from a CFO/YIG stack. As shown in Fig. 4a, b, the measured hysteresis of the CFO/YIG heterostructure repeatedly showed a sharper reversal of its out-of-plane magnetization compared to the sum of the individual CFO and YIG loops. A signature of magnetoelastic coupling was also observed by heating the CFO/YIG heterostructure to 300 °C, just above the Curie temperature of YIG (277 °C). As shown in Fig. 4c, the loop of YIG/CFO differs from that of a single CFO layer at 300 °C although the YIG no longer contributes a magnetic moment above its Curie temperature. We speculate that the higher thermal expansion coefficient of YIG imposes an in-plane strain on CFO, resulting in a magnetoelastic anisotropy favouring out-of-plane magnetization. Cooling to room temperature restored the two-step loop seen in Fig. 4a. These findings lay the foundations to discover physical coupling phenomena through simple stacking of these and many other functional oxides, choosing hetero-systems of interest from the huge library of freestanding membrane material sets enabled by various techniques.

This 3D heterostructuring technique not only offers great flexibility to design coupled multifunctional oxide films with enhanced performance, but also provides a platform to integrate various 3D and 2D material heterostructures with tailored functionalities to study novel interface phenomena. For example, we were able to tune the Fermi level of graphene with respect to its Dirac point by sandwiching it between YIG and CFO membranes. This was measured by tracking the 2D and G peaks of the Raman spectra of graphene, wherein contact with the YIG n-dopes the graphene and contact with CFO p-dopes the graphene, whereas graphene stays intrinsic when on thick hexagonal boron nitride

(hBN) (30 nm) (Fig. 4d)<sup>40</sup>. It is well known that the shift in the 2D and G peaks as well as the full-width at half-maximum (FWHM) change in the G peak correlates with the Fermi level<sup>41</sup>. As expected, a clear indication of n-doping was observed on graphene transferred onto a YIG membrane relative to the undoped graphene on hBN (blue-shift and red-shift of the 2D and G peaks, respectively, with a narrowing of the FWHM of the G peak). When graphene is sandwiched by transferring a CFO membrane on top of the graphene/YIG stack, graphene reverts back to a nearly undoped state similar to graphene on hBN (Fig. 4e-h). Such electrically coupled 2D and 3D mixed heterostructures provide a platform on which to study interfacial and proximity-induced physical couplings in 2D and 3D heterostructures, which so far has only been possible theoretically<sup>40</sup>. Combined with other conventional lift-off methods, it is now possible to couple and integrate an unprecedentedly broad range of functional single-crystalline membranes (III-V or III-N, complex oxides and 2D layered materials) on a single platform.

## Online content

Any methods, additional references, Nature Research reporting summaries, source data, extended data, supplementary information, acknowledgements, peer review information; details of author contributions and competing interests; and statements of data and code availability are available at https://doi.org/10.1038/s41586-020-1939-z.

- Spaldin, N. A. & Ramesh, R. Advances in magnetoelectric multiferroics. Nat. Mater. 18,
- Leung, C. M., Li, J., Viehland, D. & Zhuang, X. A review on applications of magnetoelectric composites: from heterostructural uncooled magnetic sensors, energy harvesters to highly efficient power converters. J. Phys. D 51, 263002 (2018).
- Bauer, U., Przybylski, M., Kirschner, J. & Beach, G. S. D. Magnetoelectric charge trap memory. Nano Lett. 12, 1437-1442 (2012).
- del Valle, J. et al. Subthreshold firing in Mott nanodevices, Nature 569, 388-392 (2019).
- Schlom, D. G. et al. Strain tuning of ferroelectric thin films. Annu. Rev. Mater. Res. 37, 589-626 (2007)
- Petrie, J. R., Jeen, H., Barron, S. C., Meyer, T. L. & Lee, H. N. Enhancing perovskite electrocatalysis through strain tuning of the oxygen deficiency. J. Am. Chem. Soc. 138, 7252-7255 (2016)
- Ahadi, K. et al. Enhancing superconductivity in SrTiO<sub>2</sub> films with strain, Sci. Adv. 5 eaaw0120 (2019)
- Bae, S. H. et al. Integration of bulk materials with two-dimensional materials for physical coupling and applications. Nat. Mater. 18, 550-560 (2019).
- Lee, H. et al. Direct observation of a two-dimensional hole gas at oxide interfaces. Nat. Mater. 17, 231-236 (2018).
- Zubko, P., Gariglio, S., Gabay, M., Ghosez, P. & Triscone, J.-M. Interface physics in complex oxide heterostructures. Annu. Rev. Condens. Matter Phys. 2, 141-165 (2011).
- Gan, Q., Rao, R. A., Eom, C. B., Garrett, J. L. & Lee, M. Direct measurement of strain effects on magnetic and electrical properties of epitaxial SrRuO<sub>3</sub> thin films. Appl. Phys. Lett. 72,
- Boota, M., Houwman, E. P., Nguyen, M. D., Lanzara, G. & Rijnders, G. Effect of fabrication conditions on phase formation and properties of epitaxial (PbMg $_{1/3}$ Nb $_{2/3}$ O $_3$ ) $_{0.67}$ -(PbTiO $_3$ ) $_{0.33}$ thin films on (001) SrTiO<sub>3</sub>. AIP Adv. 6, 055303 (2016).
- Geim, A. K. & Grigorieva, I. V. Van der Waals heterostructures. Nature 499, 419-425 (2013).
- Ahn, J. et al. Heterogeneous three-dimensional electronics by use of printed semiconductor nanomaterials. Science 314, 1754-1757 (2006).
- Yim, K. H. et al. Efficient conjugated-polymer optoelectronic devices fabricated by thinfilm transfer-printing technique. Adv. Funct. Mater. 18, 1012-1019 (2008)
- Kum, H. et al. Epitaxial growth and layer-transfer techniques for heterogeneous integration of materials for electronic and photonic devices. Nat. Electron. 2, 439-450 (2019).
- Lu, D. et al. Synthesis of freestanding single-crystal perovskite films and heterostructures by etching of sacrificial water-soluble layers, Nat. Mater, 15, 1255-1260 (2016)
- Bakaul, S. R. et al. Single crystal functional oxides on silicon. Nat. Commun. 7, 10547 (2016).
- 19 Paskiewicz, D. M., Sichel-Tissot, R., Karapetrova, E., Stan, L. & Fong, D. D. Single-crystalline SrRuO<sub>3</sub> nanomembranes: a platform for flexible oxide electronics. Nano Lett. 16, 534-542 (2016).
- 20. Ji, D. et al. Freestanding crystalline oxide perovskites down to the monolayer limit. Nature **570**, 87-90 (2019)
- Zhang, Y. et al. Flexible quasi-two-dimensional CoFe<sub>2</sub>O<sub>4</sub> epitaxial thin films for continuous strain tuning of magnetic properties. ACS Nano 11, 8002-8009 (2017).
- Kim. Y. et al. Remote epitaxy through graphene enables two-dimensional material-based layer transfer. Nature 544, 340-343 (2017).
- Kong, W. et al. Polarity governs atomic interaction through two-dimensional materials. Nat. Mater. 17, 999-1004 (2018).
- Baek, S. H. et al. Giant piezoelectricity on Si for hyperactive MEMS. Science 334, 958-961 (2011)

- Subramanian, S. et al. Properties of synthetic epitaxial graphene/molybdenum disulfide lateral heterostructures. Carbon 125, 551-556 (2017).
- 26. Coy-Diaz, H., Addou, R. & Batzill, M. Interface between graphene and SrTiO<sub>3</sub>(001) investigated by scanning tunneling microscopy and photoemission. J. Phys. Chem. C 117, 21006-21013 (2013).
- Schneider, C. W. et al. The origin of oxygen in oxide thin films: role of the substrate. Appl. Phys. Lett. 97, 192107 (2010).
- Willmott, P. R., Herger, R., Schlepütz, C. M., Martoccia, D. & Patterson, B. D. Energetic surface smoothing of complex metal-oxide thin films. Phys. Rev. Lett. 96, 176102 (2006).
- Brewer, A. et al. Uniform sputter deposition of high-quality epitaxial complex oxide thin films. J. Vac. Sci. Technol. A 35, 060607 (2017).
- 30. Chen, J. et al. Self healing of defected graphene. Appl. Phys. Lett. 102, 103107 (2013).
- Li, F. et al. Ultrahigh piezoelectricity in ferroelectric ceramics by design. Nat. Mater. 17, 349-354 (2018).
- 32. Krogstad, M. J. et al. The relation of local order to material properties in relaxor ferroelectrics. Nat. Mater. 17, 718-724 (2018).
- Li, F. et al. Giant piezoelectricity of Sm-doped  $Pb(Mg_{1/3}Nb_{2/3})O_3$ -PbTiO<sub>3</sub> single crystals. 33. Science 1, 264-268 (2019).
- Bozorth, R. M., Tilden, E. F. & Williams, A. J. Anisotropy and magnetostriction of some 34. ferrites, Phys. Rev. 99, 1788 (1955).
- Fetisov, Y. K. & Srinivasan, G. Electric field tuning characteristics of a ferrite-piezoelectric microwave resonator. Appl. Phys. Lett. 88, 143503 (2006).
- Chu, Z., PourhosseiniAsl, M. & Dong, S. Review of multi-layered magnetoelectric composite materials and devices applications. J. Phys. D 51, 243001 (2018).

- Irwin, J. et al. Magnetoelectric coupling by piezoelectric tensor design. Sci. Rep. 9, 19158
- 38. Feng, M., Wang, W., Zhou, Y., Li, H. & Jia, D. Influence of residual stress on magnetoelectric coupling of bilayered CoFe<sub>2</sub>O<sub>4</sub>/PMN-PT thin films. J. Mater. Chem. 21, 10738-10743 (2011).
- Wang, Z. et al. Domain rotation induced strain effect on the magnetic and magnetoelectric response in CoFe<sub>2</sub>O<sub>4</sub>/Pb(Mg,Nb)O<sub>3</sub>-PbTiO<sub>3</sub> heterostructures. J. Appl. Phys. 111, 034108 (2012).
- Hallal, A., Ibrahim, F., Yang, H., Roche, S. & Chshiev, M. Tailoring magnetic insulator proximity effects in graphene: first-principles calculations. 2D Mater. 4, 025074 (2017).
- Das, A. et al. Monitoring dopants by Raman scattering in an electrochemically top-gated graphene transistor. Nat. Nanotechnol. 3, 210-215 (2008).
- 42. Kim, J. & Xie, Y. H. Fabrication of dislocation-free tensile strained Si thin films using controllably oxidized porous Si substrates. Appl. Phys. Lett. 89, 152117 (2006).
- Suo, Z. & Hutchinson, J. W. Steady-state cracking in brittle substrates beneath adherent films. Int. J. Solids Struct. 25, 1337-1353 (1989).
- 44. Bu, S. D. et al. Perovskite phase stabilization in epitaxial  $Pb(Mg_{1/3}Nb_{2/3})O_3-PbTiO_3$  films by deposition onto vicinal (001) SrTiO<sub>2</sub> substrates, Appl. Phys. Lett. 79, 3482-3484 (2001)

Publisher's note Springer Nature remains neutral with regard to jurisdictional claims in published maps and institutional affiliations.

© The Author(s), under exclusive licence to Springer Nature Limited 2020

## Methods

#### Epitaxial graphene growth

Monolayer epitaxial graphene was grown via silicon sublimation from the silicon face of 6H silicon carbide (SiC (0001)) in a three-phase, hot-zone, graphite furnace (Thermal Technology LLC). In this case, a 4-inch wafer was used, and a graphite crucible was constructed to accommodate the 4-inch wafer in the furnace. The SiC was first cleaned using organic solvents (acetone, isopropyl alcohol, Nanostrip). Subsequently, the SiC is annealed in 10% hydrogen (with the rest argon) at 1,500 °C for 30 min to remove subsurface damage due to chemical and mechanical polishing. The  $\rm H_2$  was then purged from the system, and the temperature was increased to 1,800 °C for 10 min at 700 torr to form the graphene layers. This process yields low-defect-density monolayer epitaxial graphene.

#### Epitaxial complex-oxide growth

**Surface preparation.** Prior to graphene transfer and growth, the STO substrate surface was dipped in buffered hydrofluoric acid for 20 s and annealed in a furnace at 1,100 °C for 6 h. AFM was measured to ensure step-and-terrace surface morphology. MAO and GGG substrates were rinsed in acetone and isopropyl alcohol for 5 min each in an ultrasonic bath with no special surface treatment.

**Pulsed laser deposition.** STO, CFO and YIG films were grown using a pulsed-laser deposition with a KrF laser energy of 400 mJ and pulse rate of 10 Hz. Commercial ceramic or bulk single-crystal targets were used. STO was grown on top of graphene-coated (100) STO substrates at a temperature of 850 °C and an oxygen flow of 20 mtorr. The initial 500 shots to the target were made without oxygen flow to protect the graphene layer on the oxide substrate for all materials. The CFO film was grown at a temperature of 400 °C and an oxygen pressure of 10 mtorr on top of a graphene-coated (100) MAO substrate. Finally, the YIG film was grown at a temperature of 700 °C and oxygen pressure of 20 mtorr on top of a graphene-coated (111) GGG substrate. After growth, the YIG film was then post-annealed at 850 °C for 2 h under an oxygen overpressure to improve crystal quality.

**Sputtering deposition.** 90° off-axis sputtering 45 and misaligned parallel dual planar magnetron sputtering 24,29 were employed to deposit epitaxial SRO and PMN-PT films, respectively. The SRO layer (100 nm) was deposited at a temperature of 600 °C and total pressure of 200 mtorr while maintaining a 3:2 ratio of Ar and  $O_2$  gases. The PMN-PT layer (500 nm) was grown at a temperature of 625 °C under a total background pressure of 500 mtorr, maintaining a 17:3 ratio of Ar and  $O_2$ .

**MBE deposition.** BTO films were grown by MBE in a Veeco GEN10 MBE system. Molecular beams of barium and titanium were generated using a conventional effusion cell and a Ti-Ball titanium sublimation pump, respectively. The fluxes were calibrated using RHEED intensity oscillations. Barium and titanium were co-deposited onto the substrate in an oxygen background partial pressure of  $7\times10^{-7}$  torr. The substrate temperature was held at 850 °C. In situ RHEED images were consistent with the growth of smooth and epitaxial thin-film surfaces during deposition.

#### Graphene transfer

First, the graphene was exfoliated from its host SiC substrate by depositing Ni (-500 nm) as an adhesive/support layer. This was accomplished by first depositing a thin Ni layer using electron-beam evaporation (20 nm) to protect the graphene, followed by Ni sputtering at a chamber pressure of  $1\times 10^{-3}$  torr and Ar flow of 9.5 standard cubic centimetres per minute (sccm). A thermal release tape (Revalpha 319Y-4M) was then used to detach the Ni layer along with the graphene. The thermal release tape/Ni/graphene stack was directly transferred onto the oxide

substrate, and the thermal release tape was released at a temperature of 120 °C. The Ni was then etched in FeCl $_3$  solution, leaving only graphene on the oxide substrate. Finally, the sample was gently rinsed in acetone and isopropyl alcohol. This process was repeated to transfer two to three layers of graphene.

#### Ni stressor deposition

The Ni stressor layer was deposited using plasma sputtering, using a commercially bought Ni target with 99.99% purity. A thin Ti adhesive layer (20–80 nm) was deposited using electron-beam evaporation before depositing the Ni stressor. The Ni was sputtered at a chamber pressure of  $2\times 10^{-3}$  torr with 9.5 sccm of Ar flow, with a growth rate of approximately 2  $\mu m\,h^{-1}$ .

#### Characterization

**SEM, EBSD, AFM and Raman measurements.** SEM and EBSD measurements were made using a ZEISS Merlin high-resolution SEM equipped with an EBSD detector. AFM measurements were carried out using a Park NX10 AFM tool in non-contact mode. Raman spectra were obtained using a Renishaw Invia Reflex Raman confocal microscope with a laser wavelength of 532 nm, power of 1 mW and a laser spot size of 2  $\mu$ m.

**TEM measurements.** Cross-sectional TEM specimens were prepared using the focused ion beam (FEI Helios 660) technique. To prevent ionbeam damage and contamination caused by metal ions, the sample was passivated using electron-beam assisted amorphous carbon (100 nm) before using the focused ion beam. During the ion-milling process, the ion-beam energy was artificially controlled from 30 kV to 2 kV to achieve ultrathin TEM samples. Ex situ (S) TEM experiments were performed using JEOL 2010F and JEOL ARM 200CF (probe Cs-corrected) microscopes operated at 200 kV. Atomic-resolution STEM observations of epitaxial films were conducted using a JEOL ARM 200CF with a probe convergence angle of 20 mrad. A HAADF detector angle of 90-175 mrad and an annular bright-field detector angle of 11-23 mrad were used. For in situ TEM experiments, a miniature CFO/PMN-PT magnetoelectric coupled device was fabricated using the focused ion beam technique. An electron-beam assisted Pt electrode for metal probe contact was deposited onto the PMN-PT films, and the sample surface, including CFO and PMN-PT, was passivated by electron-beam induced amorphous carbon. A focused-ion-beam-cleaved specimen was connected with a metal half-grid to make the electric circuit, and this miniature device was isolated by a side-cutting method using ion milling with a low acceleration voltage of 5 kV. To remove the amorphous-carbon-assisted effect, the remaining amorphous carbon on the top of CFO was eliminated using a low-energy ion beam during the final milling stage. In situ TEM experiments were carried out using a JEOL 2010F analytical electron microscope with an acceleration voltage of 200 kV in TEM mode equipped with a biasing holder (Nanofactory Instruments AB) functionalized by a scanning tunnelling microscopy system. For electrical switching, a direct-current bias was applied inside a TEM between a sharp Pt-Ir tip operated by the scanning tunnelling microscopy function, contacting directly with the 7-nm-thick Pt layer. The TEM probe tip placement was made far from the observed CFO region (about 5 µm), with a relatively thick platinum contact region to minimize any effects from bending of the sample. Only negligible displacement of the sample was observed during in situ measurements, which also preclude any bending effects. Real-time high-resolution TEM videos were captured using a 2,048 pixel  $\times$  1,080 pixel resolution charge-coupled device (CCD) camera.

#### Magnetoelectric device fabrication

We first transferred freestanding single-crystalline PMN-PT onto a Ti-coated polydimethylsiloxane (PDMS) substrate where Ti was used as the bottom electrode, followed by fabricating a 7-nm Pt top contact on the PMN-PT. Then, the CFO membrane was directly transferred

onto the Pt-coated PMN-PT to complete the heterostructured device. The device was annealed at 150 °C overnight to remove any moisture.

#### Magnetoelectric coupling measurement

We applied a small alternating-current magnetic field at a frequency of 1 kHz on top of a direct-current magnetic field (5 kOe) in-plane across the CFO/PMN-PT device, then measured the induced voltage across the PMN-PT membrane. Voltage is generated across the PMN-PT membrane when the magnetoelastic strain in the CFO induced by the magnetic field is transferred to the PMN-PT<sup>46</sup>.

## **Data availability**

The data that support the findings of this study are available from the corresponding author upon reasonable request.

- 45. Eom, C. B. et al. In situ grown YBa $_2$ Cu $_3$ O $_7$ d thin films from single-target magnetron sputtering. *Appl. Phys. Lett.* **55**, 595–597 (1989).
- Vopson, M. M., Fetisov, Y. K., Caruntu, G. & Srinivasan, G. Measurement techniques of the magneto-electric coupling in multiferroics. *Materials* 10, 963 (2017).

Acknowledgements The team at MIT and the University of Wisconsin-Madison acknowledge support primarily by the Defense Advanced Research Projects Agency (DARPA) (award number 027049-00001, W. Carters and J. Gimlett). The work at University of Wisconsin-Madison is also supported by the Army Research Office through grant W911NF-17-1-0462. C.A.R. and J.B. acknowledge support from the SMART Center sponsored by NIST and SRC. J.A.R. and

S. Subramanian acknowledge support from NSF CAREER award 1453924. J.H.L. acknowledges

support from a National Research Foundation of Korea (NRF) grant funded by the Korea government (MSIT) (number 2018RIDIA1B07050484). The work at Cornell University is supported by the National Science Foundation (Platform for the Accelerated Realization, Analysis and Discovery of Interface Materials (PARADIM)) under Cooperative Agreement Number DMR-1539918. J.K. thanks the Masdar Institute/Khalifa University, the LG Electronics R&D Center, Amore Pacific, the LAM Research Foundation, Analogue Devices, and Rocky Mountain Vacuum Tech for general support. We are grateful to J. Li for assistance with the TEM measurements. We especially thank R. Bliem and B. Yildiz of MIT for early help in preparation of STO films.

Author contributions J.K. and C.B.E. conceived the idea and directed the team. H.S.K. designed and coordinated the experiments and characterization. H.S.K., H. Lee., S. Lindemann, W.K. and K.Q. performed epitaxial growth (pulsed-laser deposition and sputtering), characterization and heterogeneous integration development under the guidance of C.-B.E. and J.K. Epitaxial growth via MBE was performed by J.H.L. and S.X. under the guidance of D.G.S. Material characterization was done by H.S.K., P.C., L.R., S. Seo, C.C., S.-H.B. and K.L. Magnetoelectric coupling data analyses were performed by H.S.K, J.I. under the guidance of M.S.R. Device fabrication was carried out by H.S.K. and J.S. Magnetostatic and magnetoelastic data were analysed by H.S.K, S. Lee and J.B. under the guidance of C.A.R. The epitaxial graphene was grown by S. Subramanian under the guidance of J.A.R. Density functional theory calculations were performed by H. Li. All TEM imaging and analyses were performed by S.K. The manuscript was written by H.S.K., J.K. and C.B.E. All authors contributed to the analysis and discussion of the results leading to the manuscript.

Competing interests The authors declare no competing interests.

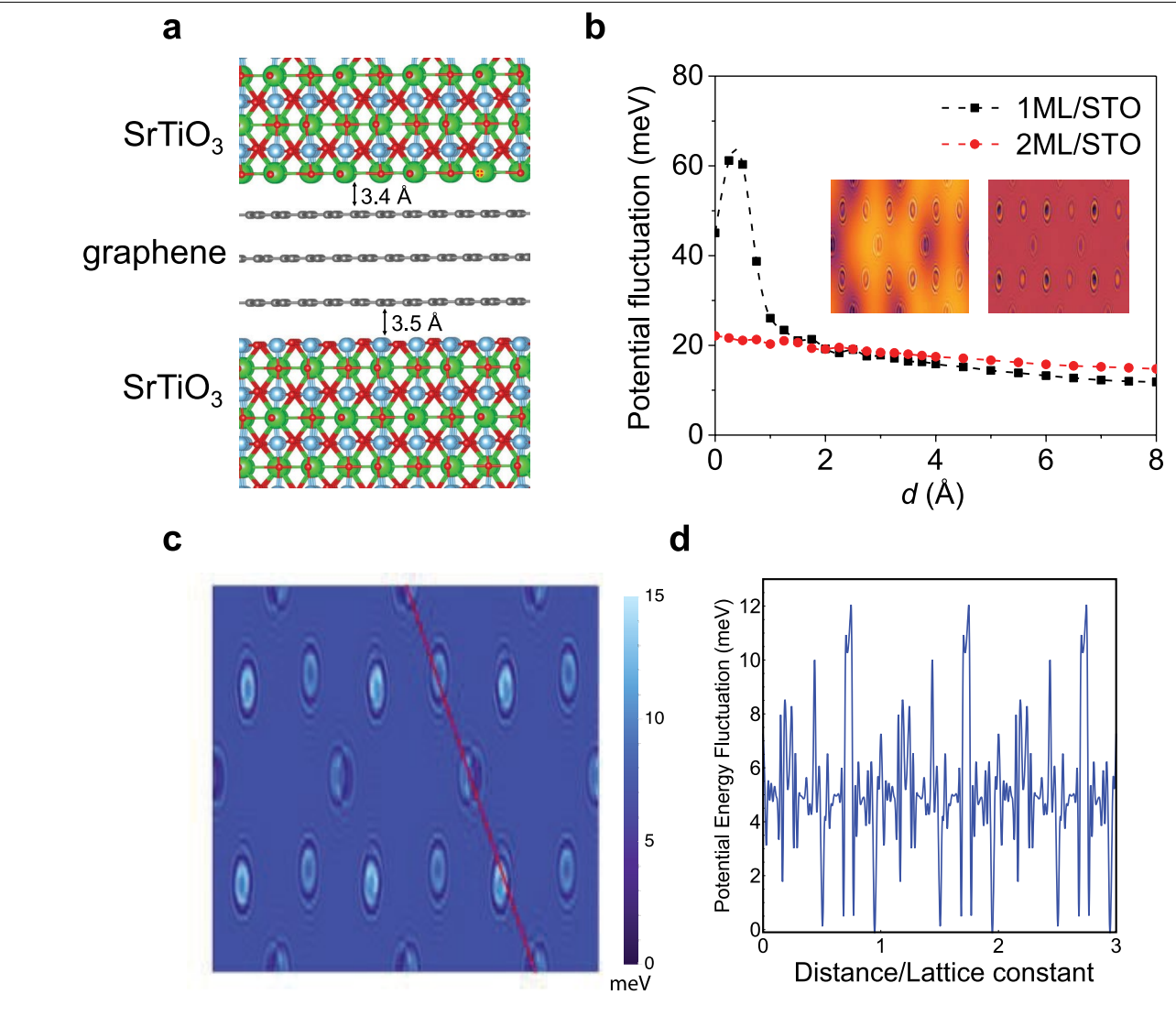
#### Additional information

**Supplementary information** is available for this paper at https://doi.org/10.1038/s41586-020-1939-7

Correspondence and requests for materials should be addressed to C.-B.E. or J.K.

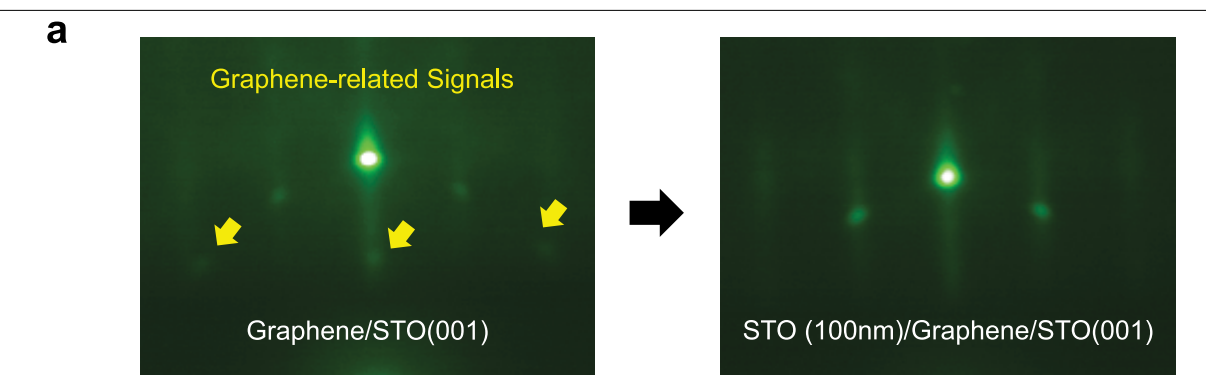
Peer review information Nature thanks Jay Switzer and the other, anonymous, reviewer(s) for their contribution to the peer review of this work.

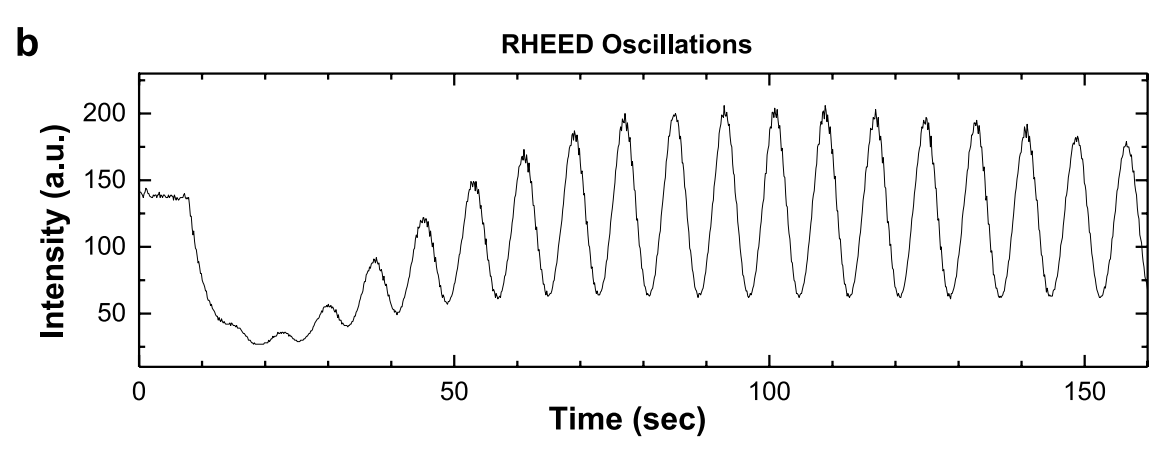
Reprints and permissions information is available at http://www.nature.com/reprints.



Extended Data Fig. 1 | Density functional theory simulation of substrate surface potential penetrating through graphene layers on a STO substrate. a, Illustration of the simulated structure. b, The potential fluctuation through graphene as a function of monolayer (1ML) and bilayer (2ML) graphene thickness d. The inset shows the potential fluctuation map on the surface of

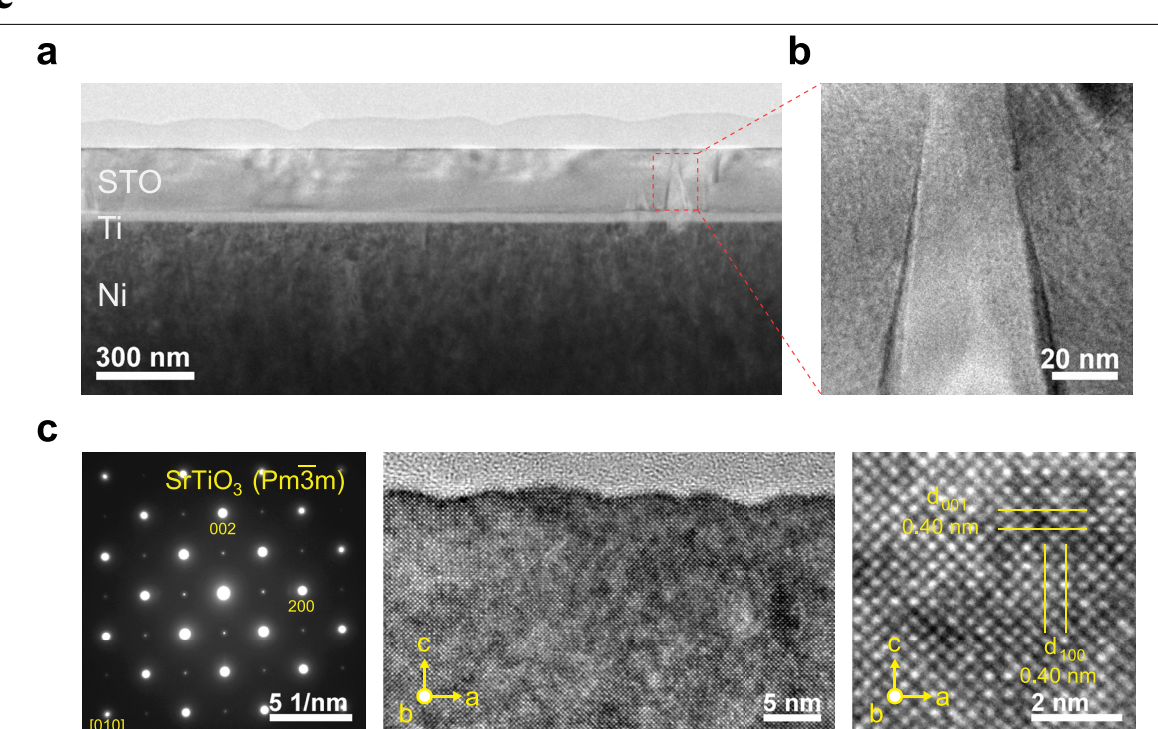
graphene-coated STO substrates for monolayer graphene (left) and bilayer graphene (right).  $\mathbf{c}$ , The potential fluctuation map (colour scale) with three monolayers of graphene on top of the STO surface.  $\mathbf{d}$ , Cross-sectional potential profile along the red line shown in  $\mathbf{c}$ .





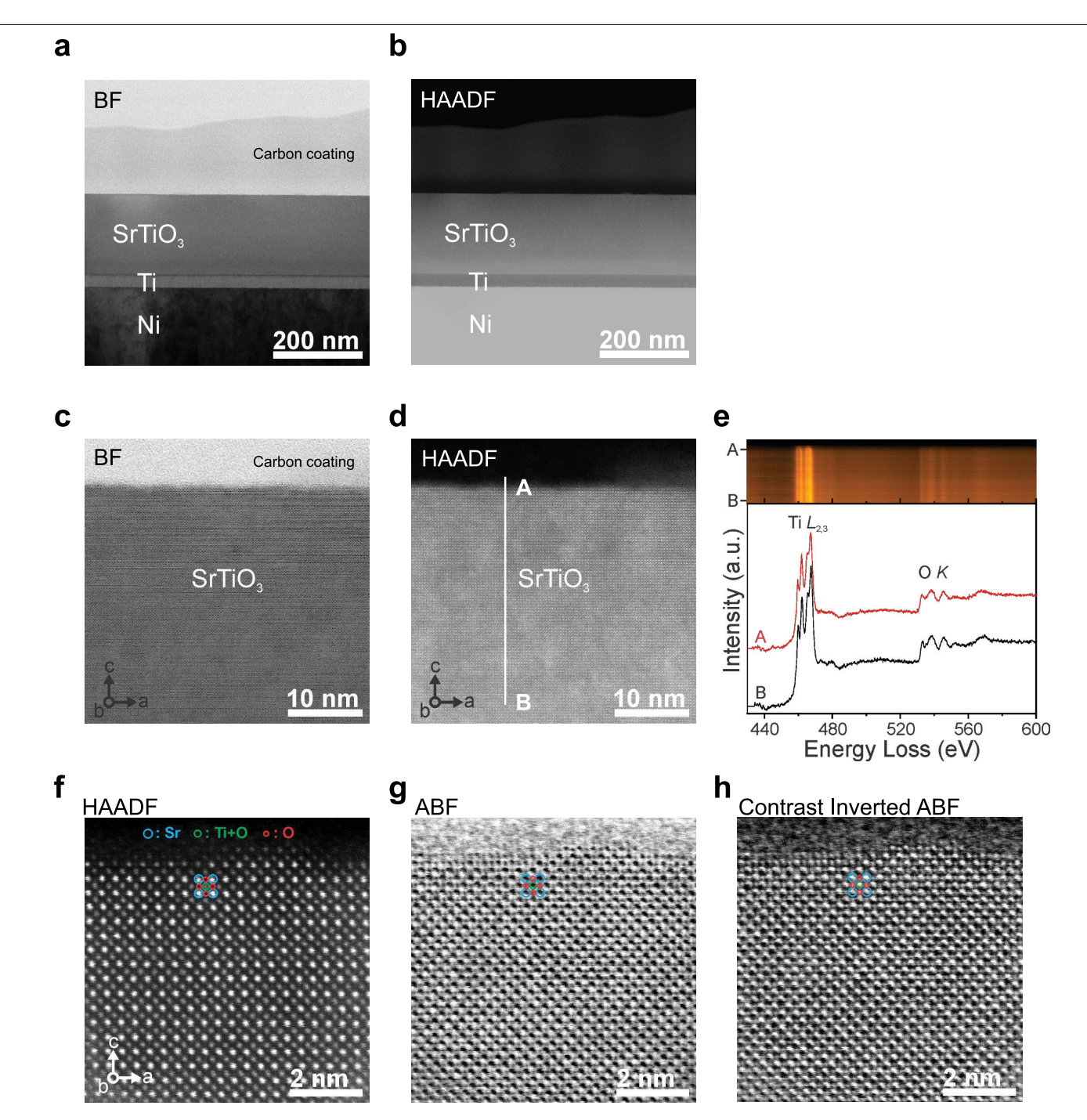
 $\label{lem:extended} \textbf{Extended Data Fig. 2} | \textbf{Pulsed-laser deposition of STO on graphene-coated} \\ \textbf{STO substrate. a}, \textbf{RHEED pattern during growth of STO on graphene-coated} \\ \textbf{STO substrate, showing crystalline growth through the entire growth process}.$ 

The yellow arrows indicate RHEED patterns caused by the transferred graphene.  ${\bf b}$ , RHEED oscillation during the growth of STO on the graphene-coated STO substrate.



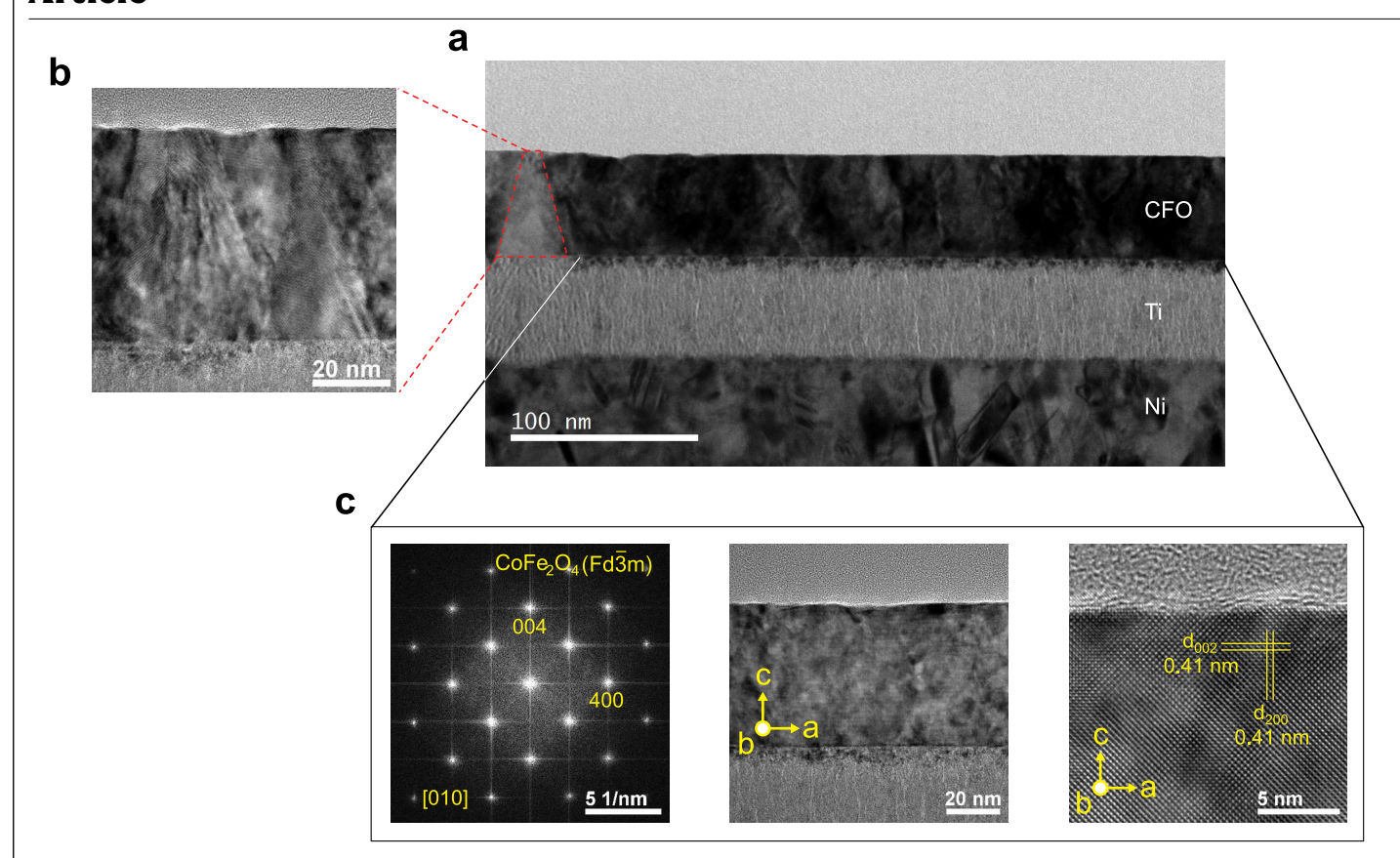
 $\label{lem:extended} \textbf{Extended Data Fig. 3} | \textbf{Cross-sectional TEM analysis of exfoliated STO} \\ \textbf{membrane. a}, \textbf{Low-magnification TEM image of STO membrane supported by} \\ \textbf{the Ni stressor layer. b}, \textbf{Zoom-in of polycrystalline domains caused by residues} \\ \textbf{left on graphene after transfer. c}, \textbf{High-resolution TEM image of the STO} \\ \\$ 

membrane (centre), with selected area electron diffraction (left) and high-resolution TEM (right) images, confirming the overall single-crystallinity of the membrane. The single-crystalline STO membrane has a cubic structure in the  $Pm\overline{3}m$  space group with lattice distances  $d_{100}$  and  $d_{001}$  of 0.4 nm.



**Extended Data Fig. 4** | **STEM analysis of the SrTiO** $_3$  **buffer layer grown in vacuum. a**, and **b**, show the bright-field (BF) and HAADF-STEM images of the exfoliated STO membrane (the same TEM sample as shown in Extended Data Fig. 3) at low magnification, respectively. **c** and **d** show higher-resolution bright-field and HAADF-STEM images of the sample, respectively. **e**, Electron energy loss spectroscopy spectra and line profile from the exfoliated surface to the bulk region (A–B in **d**), verifying that the composition of the buffer layer

grown in vacuum is identical to the region grown under oxygen overpressure.  $\textbf{f}, \textbf{High-resolution HAADF}, \textbf{showing individual atoms of the STO membrane at the exfoliation surface (the region grown in vacuum). The annular bright-field (ABF) and contrast inverted annular bright-field images (<math>\textbf{g}$  and h, respectively) clearly show the absence of oxygen vacancies and no discernible differences are observed between the regions grown in vacuum and in oxygen.

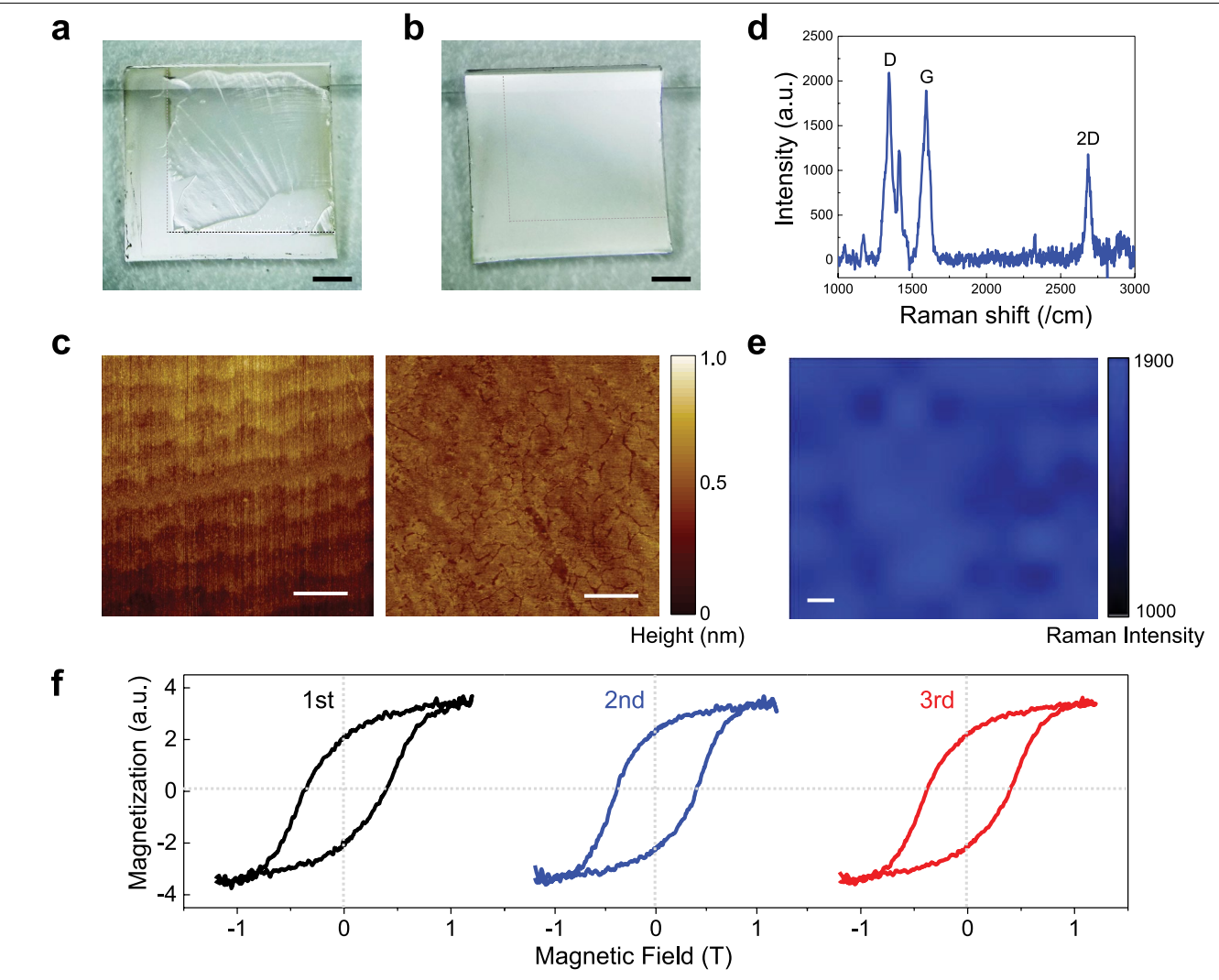


**Extended Data Fig. 5 | Cross-sectional TEM analysis of exfoliated CFO membrane. a**, Cross-sectional TEM of exfoliated CFO on the Ti/Ni stressor layer. The red dotted line indicates a polycrystalline domain caused by residues left during graphene transfer. **b**, Zoomed-in TEM of the polycrystalline area marked by red dotted lines. **c**, Higher-resolution cross-sectional TEM of the

CFO film (centre), with selected area electron diffraction (left) and high-resolution TEM (right) images, confirming the overall single-crystallinity of the membrane. The single-crystalline CFO membrane has a cubic structure in the  $Fd\overline{3}m$  space group with a lattice distance  $d_{200}$  and  $d_{002}$  of 0.41 nm.

**Extended Data Fig. 6** | **Exfoliation and characterization of BaTiO**<sub>3</sub> membrane **grown via MBE. a**, Photograph of exfoliated BTO membrane (50 nm) grown via remote epitaxy. **b**, EBSD of the exfoliated BTO membrane showing single-

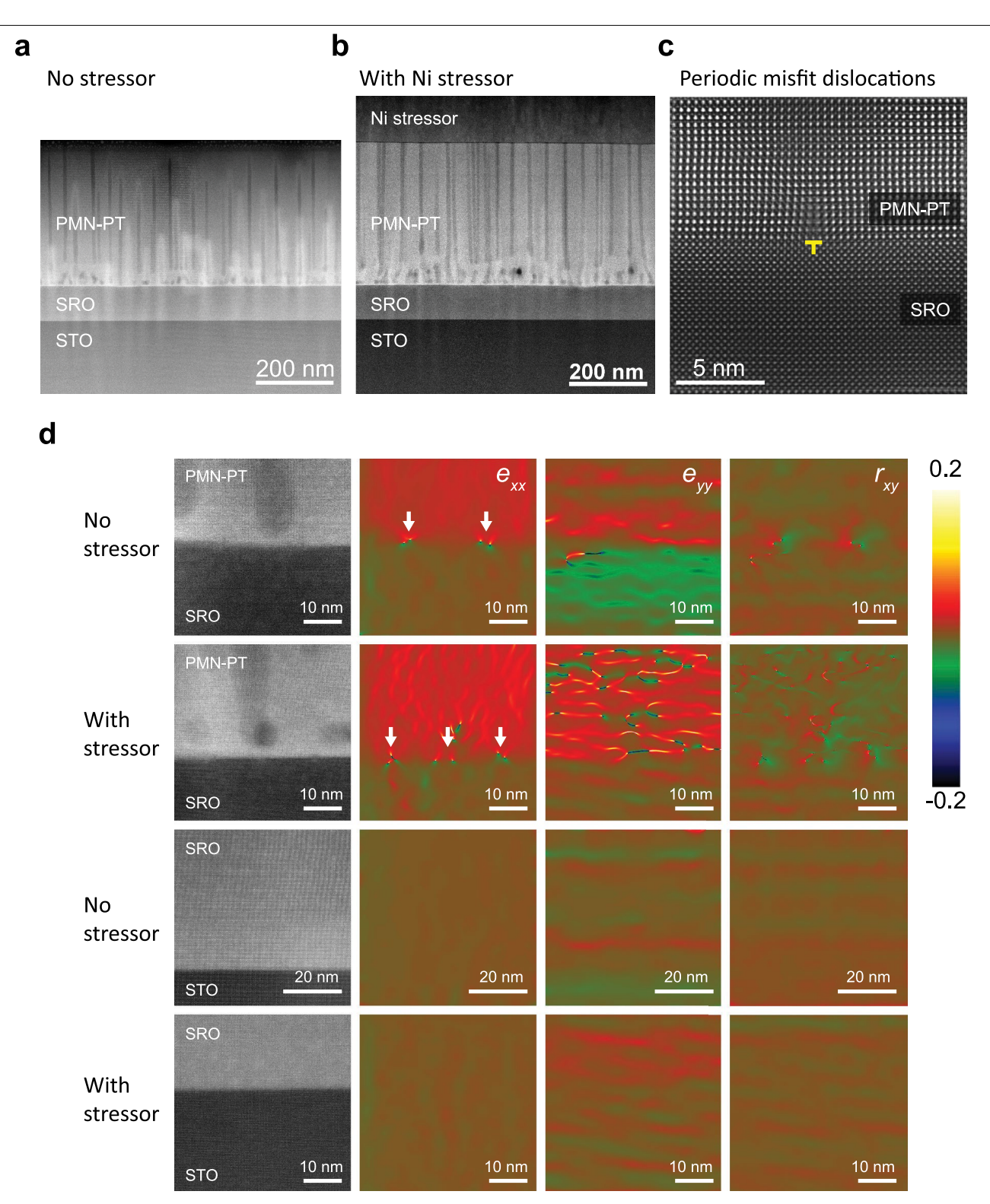
crystalline (100) orientation.  $\mathbf{c}$ , The inverse-pole map of the EBSD data shown in  $\mathbf{b}$ .  $\mathbf{d}$ , Electron backscattering patterns (also known as Kikuchi patterns) of the BTO membrane seen over the entire area of the sample.



#### Extended Data Fig. 7 | Reusability of a graphene-coated MAO substrate.

 $\label{eq:absolute_problem} \textbf{a}, \textbf{b}, \textbf{Microscope} images of a MAO substrate after exfoliating a CFO film grown on monolayer (\textbf{a}) and bilayer (\textbf{b}) graphene, where severe damage on the surface of the MAO substrate after exfoliation of CFO grown on monolayer graphene was observed, caused by crack propagation into the substrate. No evidence of damage was observed on substrates coated with bilayer graphene because the second graphene transfer covers the macroscopic defective areas of the first graphene layer. The scale bar indicates 1 mm. <math display="block">\textbf{c}, \textbf{AFM} \ \text{of the pristine MAO}$  substrate surface (left) and after one cycle of CFO exfoliation (right) with a root-mean-square roughness of approximately 5.5 Å before and after exfoliation. Scale bar indicates 1 µm. d, e, Raman spectra showing the characteristic D peak,

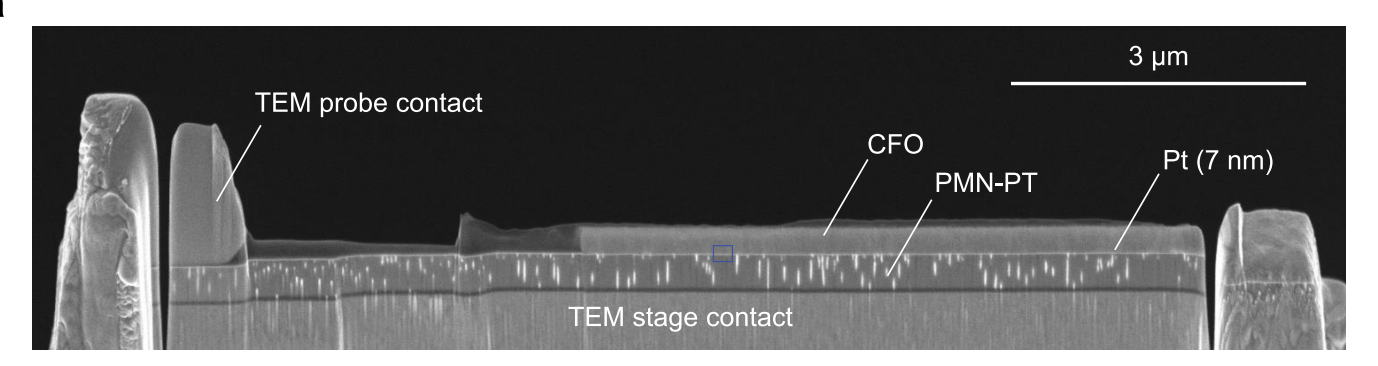
G peak and 2D peak of graphene (**d**) and Raman intensity mapping (**e**) of the 2D peak (2,685 cm<sup>-1</sup>) of graphene on the MAO substrate after one cycle of CFO exfoliation, showing evidence that graphene is preserved on the MAO substrate after exfoliation, probably because the non-specific adhesion between graphene and CFO is weaker than that between graphene and MAO. Where this is not the case, we could etch off any graphene remaining on the substrate and re-deposit graphene before epitaxy. The scale bar indicates 10  $\mu$ m. **f**, Magnetic hysteresis *M* of the three exfoliated CFO membranes produced on a single graphene-coated MAO substrate measured by vibrating sample magnetometry at room temperature. a.u., arbitrary units.



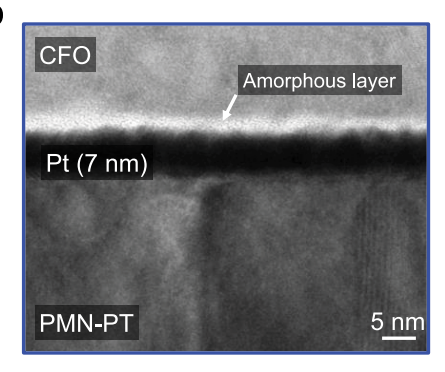
**Extended Data Fig. 8 | STEM imaging and strain analysis of the PMN-PT/SRO/STO interfaces. a, b,** Cross-sectional HAADF-STEM images of the PMN-PT/SRO/STO interfaces with and without a Ni stressor layer. Clear straining at the PMN-PT/SRO interface can be seen with a Ni stressor layer, whereas the SRO/STO interface remains unstrained. **c,** Atomic-resolution STEM image of one of the periodic edge dislocations observed at the PMN-PT/SRO interface.

 ${f d}$ , Geometric phase analysis of the PMN-PT/SRO and SRO/STO interfaces in the x direction (2nd column), y direction (3rd column) and rotational geometry (last column) with and without the Ni stressor layer. The white arrows indicate edge dislocations. The colour scale indicates the strain fraction with reference to the SRO substrate.

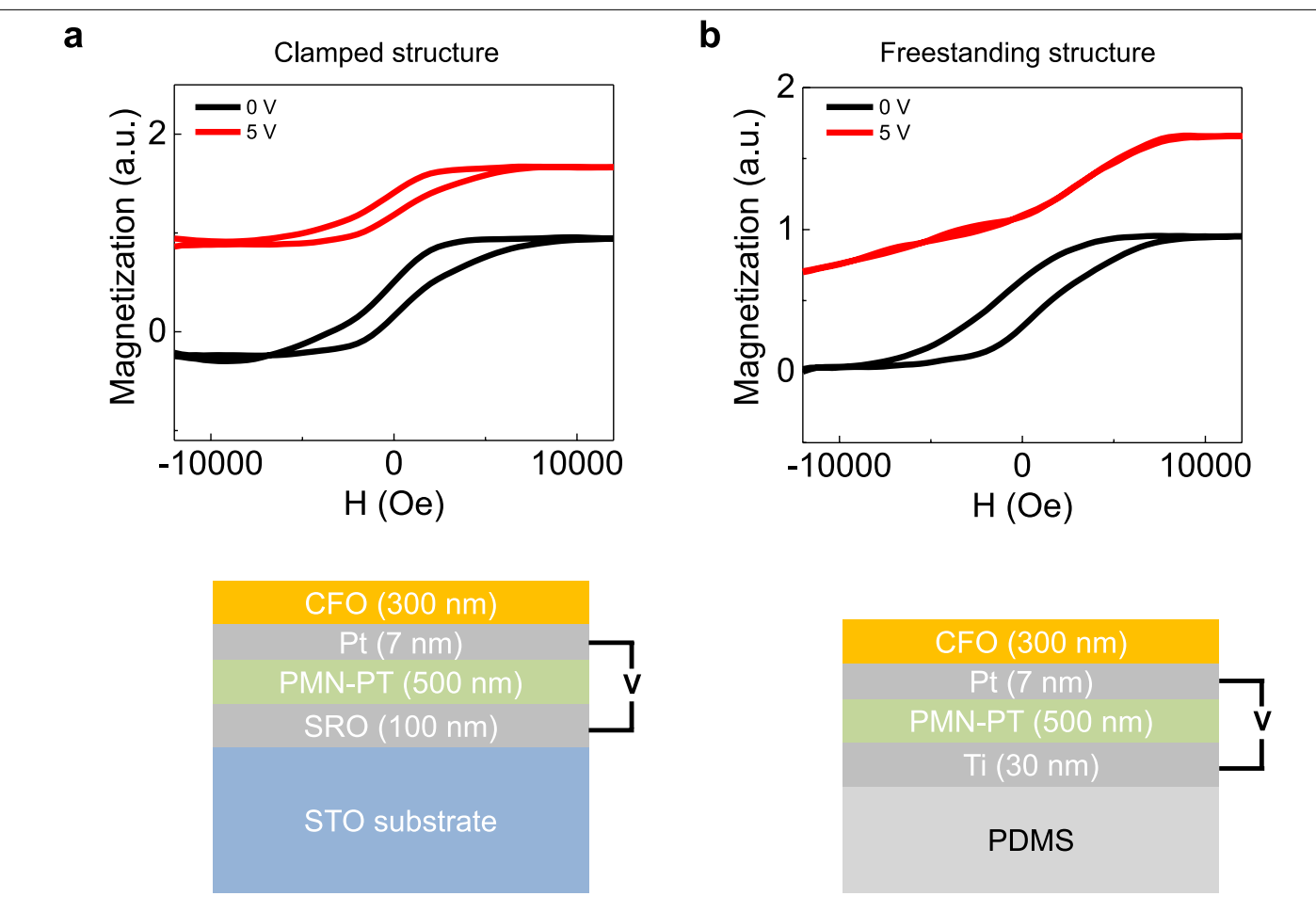
a



b



much thicker and further away from the actively observed region (distance greater than 5  $\mu m$ ) to prevent effects caused by bending of the sample.  $\boldsymbol{b}$ , High-resolution TEM image of the CFO/Pt/PMN-PT interface, showing a thin amorphous oxide layer that has formed between the CFO and Pt, enabling efficient strain coupling.



**Extended Data Fig. 10 | CFO magnetic hysteresis as a function of voltage applied across PMN-PT.** CFO magnetism with a varying voltage bias across a PMN-PT measured via vibrating sample magnetometry. **a**, In the clamped structure, the PMN-PT film is grown on a SRO/STO substrate, and the CFO

membrane is transferred on top of a thin Pt layer deposited on top of PMN-PT.  $\mathbf{b}$ , In the freestanding structure, the PMN-PT membrane is transferred onto a PDMS substrate after exfoliation. The rest of the stack is identical.